Performance Evaluation of Aeronautical Cables in Semi-Coaxial Geometries: A Novel Test Approach

Sofia P. Mavidou, *Student Member, IEEE*, David Clark, *Member, IEEE*, Michail Michelarakis, *Member, IEEE*, Christopher Stone and A. Manu Haddad, *Member, IEEE*

***Abstract*— This study examines the Partial Discharge (PD) performance of aircraft cables using a specially designed test electrode. Electrode positioning was precisely controlled within an atmospheric chamber to replicate coaxial geometries. Long exposure imaging reveals useful insights that enhance our understanding of PD behaviour at varying atmospheric pressure. The research compares the experimental data with existing mathematical models based on the Paschen and Halleck equations revealing notable inconsistencies, particularly at higher pressures. This work contributes valuable insights into the complexities of PD phenomena in aircraft cables and proposes a new model by enhancing an existing predictive model and incorporating the influence of an insulation barrier.**

***Index Terms*— Aerospace applications, aircraft cabling, coaxial geometries, EWIS, long exposure imaging, more-electric aircraft, partial discharges.**

I. Introduction

As national and global economies strive for net-zero carbon emissions, the aviation industry is experiencing a significant transformation towards more-electric aircraft (MEA). This electric transition not only supports the global sustainability agenda but also introduces unique challenges, particularly in the design and reliability of electrical systems [1]-[3]. A crucial aspect of this challenge lies in understanding and controlling Partial Discharge (PD) within aircraft electrical systems, a phenomenon that can significantly impact the overall safety and functionality of MEAs [4].

The increase of aircraft system voltages due to increasing load electrification, coupled with the unique nature of the aircraft environment characterized by confined spaces, restricted access, and intricate cable routing, amplifies the complexity of cable maintenance and repair procedures. This complexity necessitates an examination of the PD performance of cables, particularly considering that PDs occurring at low pressures may exhibit harmful potential due to their higher energy release [5]. PD events can be indicators of potential cable failures, emphasizing the importance of detection and mitigation [6]. However, the presence of PD may be obscured by the surrounding electrical noise, making their identification a complex task.

This study focuses on approximating the conditions of cables in trays or metal ductwork on aircraft using a geometry that is comparatively straightforward to analyse mathematically. Coaxial cylinder geometries have been investigated in the literature [7] - [10] and well - known models have been derived such as Peek's formulae.

In this study, three aeronautical grade cables are methodically investigated for their PD performance: two with extruded insulation and one with tape-wrapped insulation, under varying pressures to simulate different flight altitudes. The temperature is kept constant within the range of 20-21ºC. Focusing on aircraft cables exposed to high voltage in coaxial geometries, the study conducts tests with varying separations between the cable and a specially designed ground electrode. The investigation primarily explores PD phenomenology in semi-coaxial configurations, rather than addressing specific operational stresses or application scenarios. The findings reveal insights into the relationship between Partial Discharge Inception Voltage (PDIV) and Partial Discharge Extinction Voltage (PDEV), pressure, and voltage. The work also highlights the challenges of applying current mathematical models to predict PDIV in coaxial geometries and suggests a model that incorporates the insulation thickness of the cable.

II. Methodology

Details of the test electrode design and experimental setup are presented in this section.

A. Test Electrode Design

The test electrode was designed to ensure coaxial field

Manuscript received 28 February, 2024; revised 21 December, 2024; accepted 02 January, 2025.

Sofia P. Mavidou (e-mail: MavidouS@cardiff.ac.uk), David Clark (e-mail: ClarkD@cardiff.ac.uk), Michail Michelarakis (e-mail: MichelarakisM@cardiff.ac.uk), Christopher Stone (e-mail: StoneCT1@cardiff.ac.uk) and Manu Haddad (e-mail: Haddad@cardiff.ac.uk) are with the Advanced High-Voltage Engineering Research Centre, Cardiff University CF24 3AA, Cardiff, UK.

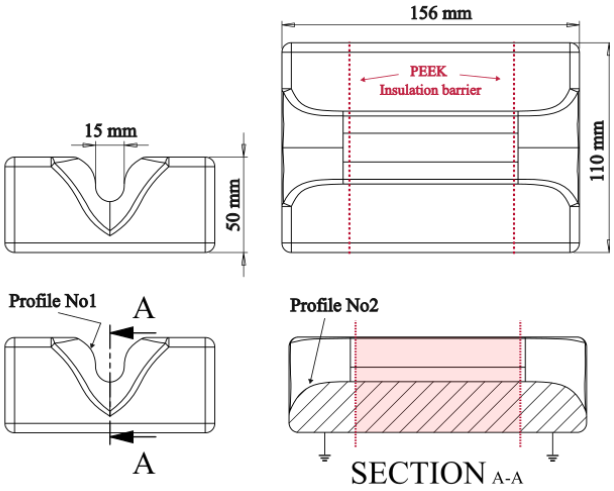

Fig. 1. Electrode schematic with different views and dimensions, showing the two profiles, the cut point locations, and the PEEK insulation barriers.

TABLE I
ROGOWSKI PROFILE VALUES

	Profile No1	Profile No2
α	15	20
v	$\pm\pi/2$	$\pm\pi/2$

distribution about the energized cable, while maintaining visibility of the test for cameras and other optical measurement systems. It allows for an investigation into the PD performance of aerospace cables examining their behaviour as they deviate from or approach the coaxial position.

A single billet of aluminium was machined, partitioned at two locations, and reassembled with PEEK insulating sheets, each with a thickness of 50µm, laser cut to align with the electrode profile, ensuring uninterrupted geometry. Fig. 1 illustrates the dimensions of the ground electrode and identifies the two distinct Rogowski profiles used in its design, and the specific cut points for partition of the electrode. The two end sections of the electrode were directly grounded, while a precision 50 Ω shunt resistance was connected between the middle section and ground to capture PD electrical signals.

The parameters for the profiles and the locations of the cut points were determined following detailed simulations. The electric field magnitude along Profile No2 is shown in Fig. 2. Although the value decreases at the ends of the electrode, the strategically placed cuts serve a crucial function, ensuring a symmetric field distribution along the span of the sensing electrode.

The Rogowski profile equations are given by (1) [11]:

$$x(u) = \left(\frac{a}{\pi}\right) * (u + 1 + e^{u} * \cos(v))$$
$$y(u) = \left(\frac{a}{\pi}\right) * (v + e^{u} * \sin(v)) \quad (1)$$

The values used for the two profiles are given in Table I.

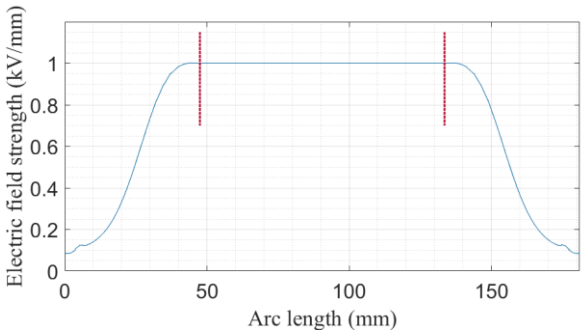

Fig. 2. Electric field magnitude along profile No2. Simulations for conductor diameter 2mm and 2mm offset from electrode energized at 2kV.

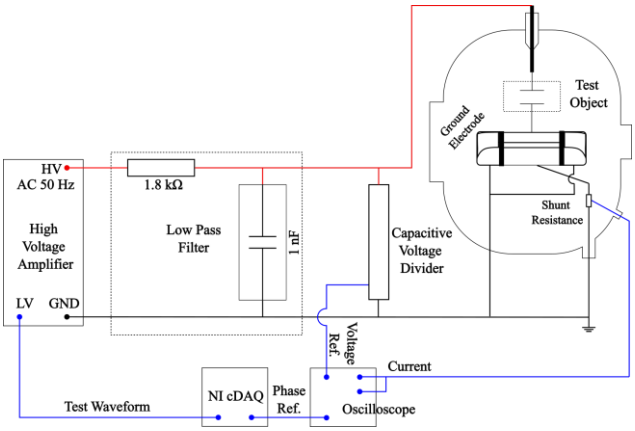

Fig. 3. Experimental setup schematic.

B. Experimental Setup

A partial discharge test circuit was constructed to the general guidelines of BS EN 60270 [12], as shown in Fig. 3. The test voltage waveform was generated by a DAQ output module and subsequently amplified by a high voltage amplifier, achieving a gain of 3000 V/V. The applied voltage was monitored using a voltage divider with a ratio of 1000:1 with a capacitance of 8.3 pF. A low pass filter with cutoff frequency of 88.4 kHz was formed by adding a series resistance of 1.8 kΩ between the high-voltage source and coupling capacitor of 1 nF.

The test configuration shown in Fig. 4 is placed inside a vacuum rated controlled-atmosphere test chamber. Motorized linear and vertical translation stages, with travel ranges of 50 and 20 mm respectively, were used to control the movement of the electrode achieving different positions in relation to the cable as shown in Fig. 5.

The grounded electrode was mounted on the stages and fixed in position with reference to the cable. The voltage was applied to the cable under test through a copper conductor with a diameter roughly five times that of the cable, ensuring sufficiently low magnitude electric field away from the test object. The coupling between the copper conductor and the edge of the cable specimen under test was performed through a stainless-steel sphere of 50.8 cm diameter. In that way, a sufficiently low electric field magnitude is achieved at this joint point. The cable was securely fixed and tensioned between the two spheres.

A 50Hz AC voltage was continuously applied and ramped

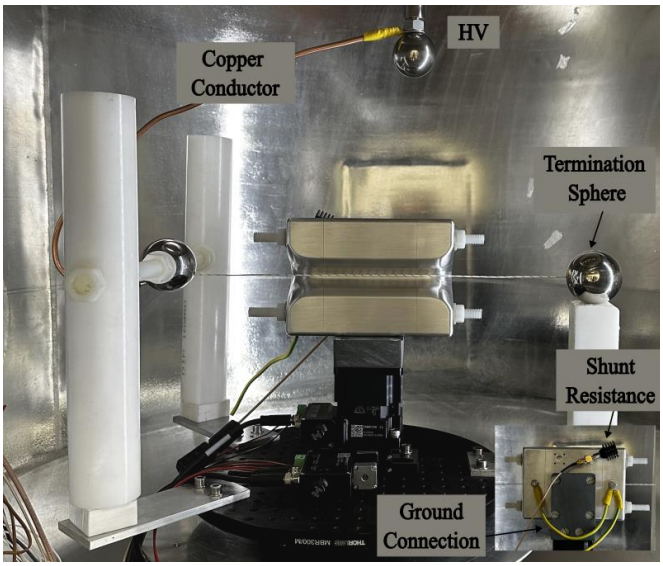

Fig. 4. Test configuration inside the atmospheric test chamber: Cable under test tensioned between field grading spheres and connected to the terminal of the HV bushing. Electrode mounted on XZ motorised stage with insulated supports. Inset: ground and shunt resistance connections.

at 100 V/s for test voltages below 5 kV. For test voltages above 5kV, the rate of increase was adjusted to ensure the total test times remained below 50 seconds. Specifically, the ramp rate of the signal fed to the amplifier was increased to ensure that the rise and fall of the test voltage occurred within the set time of 50 seconds. In the absence of detailed testing methods from international standards specific to aerospace applications and PD testing, a maximum voltage application duration of 50 seconds was selected to ensure that the insulation would not be excessively stressed. It should be noted that a sensitivity check was conducted, and it was observed that, within the range of rate-of-rise values examined, the PDIV value remained unaffected. The voltage was raised until it met the condition defined in the BS EN 3475 standard [13] as "the lowest voltage at which continuous (steady state with a minimum of 1 detected Partial Discharge per second for at least 10 seconds) partial discharges occur as the applied voltage is increased."

To ensure that the PD source in the tests was exclusively the cable-electrode arrangement, the cable was initially arranged at a sufficient distance from the electrode, ensuring that no PD would occur. The voltage was gradually increased, and no PD activity was detected under these conditions. Without altering any other aspects of the setup, the cable was subsequently moved closer to the electrode, and PD activity was observed. This procedure ensured that the platform layout reliably isolated the cable-electrode arrangement as the sole source of PD, minimizing interference from external noise or other discharge sources. A viewport on the side wall of the atmospheric test chamber was used to capture long-exposure images with a Nikon D7200 camera.

The experimental setup encompassed five distinct positions, as illustrated in Fig. 5, each representing a different configuration for the cable under test.

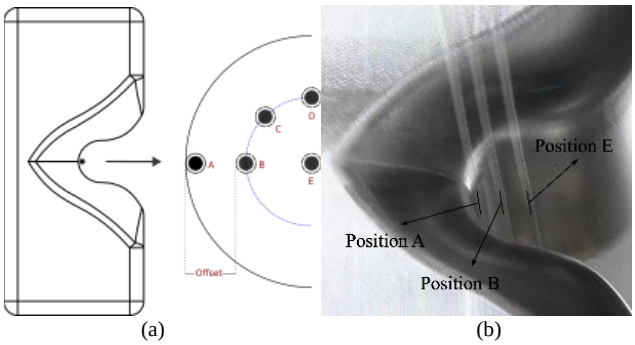

Fig. 5. Different positions (a) schematic and (b) image showing the positions of the cable in reference to the electrode.

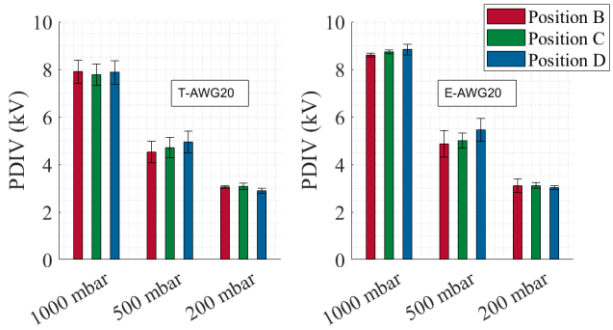

Fig. 6. Comparison of B, C and D positions for T-AWG20 and E-AWG20 for all pressures.

Position A is defined by the cable being attached directly to the grounded electrode, having no offset from it.

Position B represents a 3 mm linear offset from the grounded electrode, creating an air gap between the cable and the electrode.

Positions C and D sit at 45° and 90° offsets along a circular arc passing through Position B, maintaining a 3mm electrode spacing.

Position E mimics true coaxial positioning, where the cable and the grounded electrode half-circle share the same centre.

The positions B, C, and D were expected to yield equivalent PDIV results due to consistent spacing between cable and electrode, thereby validating both the design and the precision movement of the system.

The movements of both the linear and vertical translation stages were remotely controlled from a PC outside the cage. This approach eliminates the need to interfere with the experimental setup, ensuring that all test conditions remained consistent throughout the testing process.

III. Results and Discussion

In the plots presented in this work, the type of insulation is designated as 'E' for extruded and 'T' for tape-wrapped. The AWG specification is included in the identifier of each cable.

The key dimensions of the tested cables are as follows:

- E-AWG20: t_d = 0.18 mm, d_c = 1.01 mm
- E-AWG22: t_d = 0.18 mm, d_c = 0.81 mm
- T-AWG20: t_d = 0.185 mm, d_c = 0.97 mm

Where t_d is the insulation thickness and d_c is the core diameter.

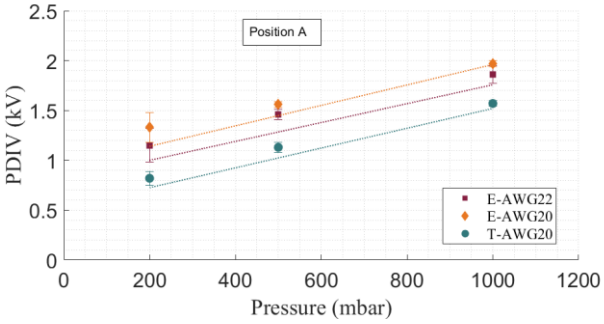

(a)

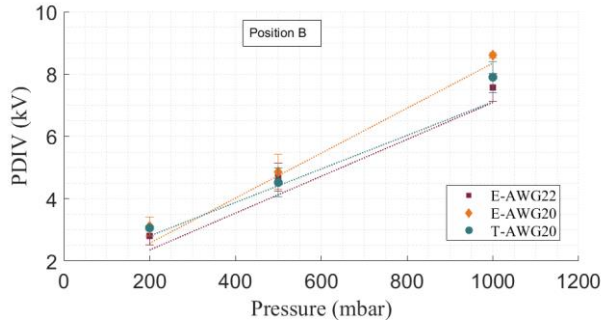

(b)

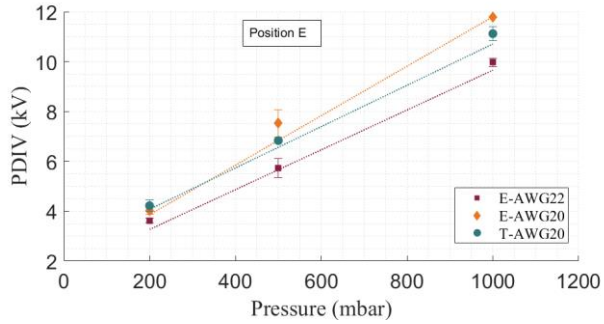

(c)

Fig. 7. PDIV values with trendlines based on minimum values for varying pressure for all cables for position (a) A, (b) B and (c) E.

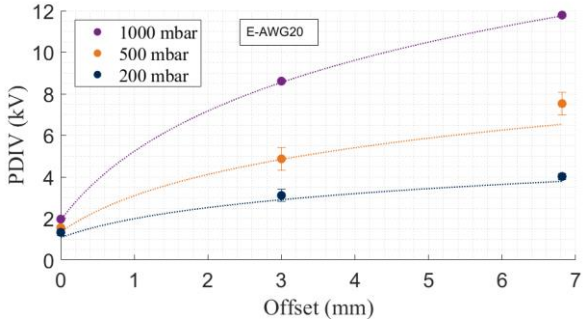

(a)

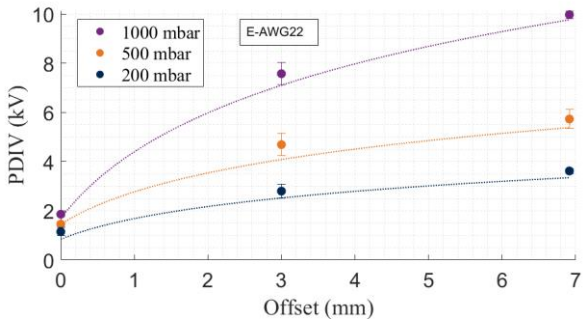

(b)

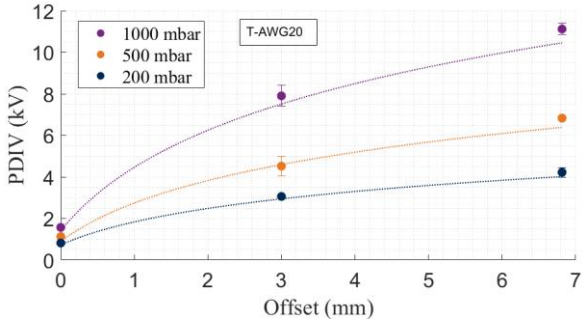

(c)

Fig. 8. PDIV values with trendlines based on minimum values for varying offset for all pressures for cables (a) E-AWG20, (b) E-AWG22 and (c) T-AWG20.

A. PD Evaluation

As the first step in validating the system's accuracy, two cables were tested at positions B, C, and D, all with the same offset from the ground electrode. The selected cables had identical AWG specification; one featured extruded insulation, and the other had tape-wrapped insulation. As expected, the PDIV for each of the cables, tested in three different positions, showed consistent results, as depicted in Fig. 6. This indicates that the behaviour of each cable was uniform across all tested positions. Five tests were conducted for each case, and the standard deviation of these results is also depicted in the plots. Tests were conducted at pressures of 1000, 500, and 200 mbar, corresponding to different flying altitudes. The larger standard deviations observed at 500 mbar could be attributed to the inherent PD variability observed at low pressures due to the largen mean electron free path and may be mitigated with a higher number of tests.

After validating the accuracy of the measurement system, the three cables were tested at pressures of 1000, 500, and 200 mbar for positions A, B, and E, with the results presented in Fig. 7 (a)-(c). The mean PDIV value and standard deviation for these tests is displayed in the plots, and fitted curves are also plotted to illustrate the trend of the results, facilitating easier comparison with established equations in the next section. It should be noted that the fitted curves in Figures 7, 8, and 9 are based on minimum values rather than averages to highlight that the lower error bounds are not significantly different from the minimum values. The results clearly show a linear trend for all cables, with the PDIV increasing as the pressure rises. As expected and is previously shown in [14], the cables with extruded insulation exhibit better PDIV performance.

The results presented in Fig. 8 are for the different positions examined varying pressure levels for all three cables. This time, an increase in offset results in PDIV values following a different trend, that is a logarithmic one. This observed trend may be attributed to the coaxial geometry involved in the experiment, compared with a simpler geometry such as a plane

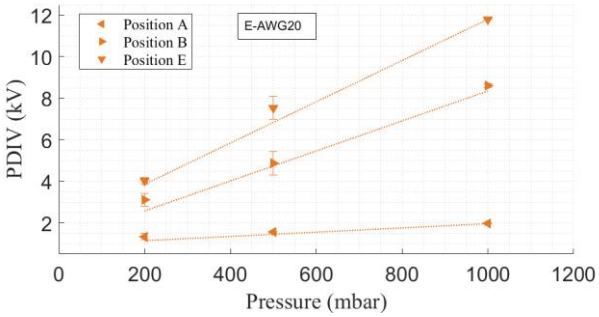

Fig. 9. PDIV values with trendlines based on minimum values for varying pressure for E-AWG20 and all positions.

electrode and a cable at varying air gaps.

Another observation that can be made from the results shown in Fig. 9 indicates that different positions exhibit different sensitivities to pressure. When the cable is placed at Position E, increasing pressure results in a bigger increment in the PDIV value compared to when the cable rests on the electrode, i.e. when it is at Position A. Another statement for the same observation could be that, at higher pressures, the distance from the ground electrode has a bigger impact on PDIV compared with lower pressure. Proximity to the electrode (Position A) might result in a more distorted field, making PDIV less sensitive to pressure changes.

From Figures 7-9, it can be concluded that increasing pressure and increasing offset both lead to an increase in PDIV. However, two distinct trends, linear and a logarithmic, are evident for each variable within this specific geometry. Therefore, these trends may necessitate separate examinations.

PDEV was also evaluated. After the voltage was increased to the maximum test voltage and PDIV was obtained, the voltage was decreased at the same rate and PDEV was determined. Representative results are presented in Table II for a pressure level of 200 mbar, concerning two cables at three different positions. The observed PDEV values are lower than their corresponding PDIV values in all cases. This phenomenon is potentially hazardous to the system as there is a risk for sustained PD which can degrade insulation over time, leading to premature failure.

B. Long Exposure Imaging

Long exposure images of the E-AWG22 cable tests were captured using a Nikon D7200 camera, with settings of 25 seconds exposure, ISO 2000, and an aperture of f/5.6. Having determined the PDIV for each combination of position and pressure, additional tests were performed at PDIV and PDIV+20%, with the voltage held constant over the duration of the camera exposure. Fig. 10 illustrates the initial images captured for positions A and E at PDIV + 20% levels and 200 mbar. A bright field image is also included for reference. While these images demonstrate that PD can be optically detected from this perspective, they also reveal substantial reflection within the grounded electrode's channel, resulting in an image that is not entirely clear. Nevertheless, these images are significant as they confirm that the cut points on the electrode

TABLE II
PDIV AND PDEV VALUES FOR DIFFERENT POSITIONS AT 200 MBAR

	E-AWG20		T-AWG20	
	PDIV (kV)	**PDEV (kV)**	**PDIV (kV)**	**PDEV (kV)**
Position A	1.33	0.78	0.82	0.70
Position B	3.11	2.95	3.06	3.02
Position E	4.02	3.96	4.22	3.92

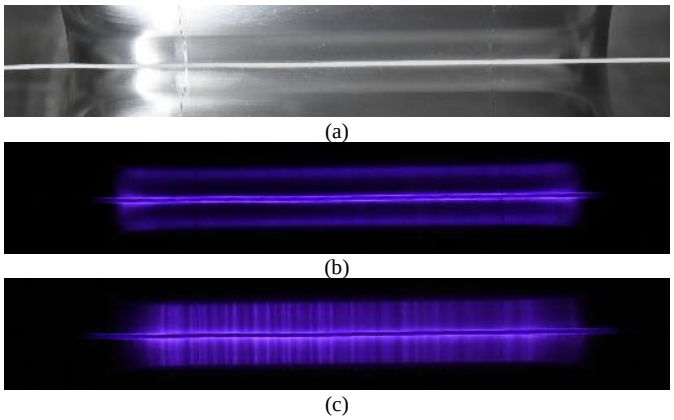

(a)

(b)

(c)

Fig. 10. Initial images captured showing (a) cable-electrode configuration and long exposure images for 200 mbar and PDIV +20% at position (b) A and (c) E.

do not disrupt the geometry and, consequently, the electric field distribution.

The remaining long exposure images, depicted in Fig. 11, Fig. 13 - Fig. 16 were captured from a different angle to eliminate reflection. The bright field image is included for reference, illustrating the PD activity during the exposure time. To enhance clarity, a very low opacity overlay of the bright field image was placed on the long exposure images.

The Nikon D7200 captures images within the visible spectrum, which is suitable for visualizing PD activity. However, PD phenomena often emit ultraviolet (UV) and infrared radiation (IR), which can provide more sensitive detection. Future studies utilizing UV or IR imaging could enhance detection accuracy and reveal additional insights, particularly for early-stage PD detection, which is critical for system reliability.

Fig. 11 displays the activity of PD at Position A for varying pressures with the same applied voltage. It is observed that reduced pressure levels result in increased energy levels, hence a more illuminated area adjacent to the cable. This phenomenon is further discussed later. It should be noted that for 1000 mbar, even though no activity was visually captured by the camera, partial discharges were indeed detected by the electrical detection method. An example of these pulses undetected by the camera can be seen in Fig. 12. The figure presents pulses captured using segmented triggering, which are sequential in acquisition but not in real time. While the pulses are plotted adjacent to each other, the x-axis represents segments rather than actual time. The time window for these acquisitions was set at 2 μs, denoted as τ_s. A more sensitive optical system could

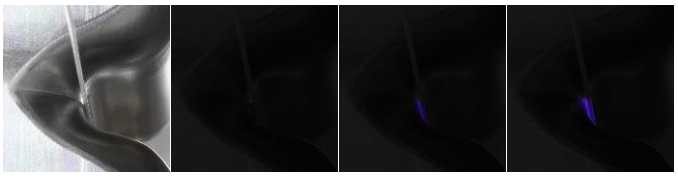

(a) (b) (c) (d)

Fig. 11. Position A (a) bright field image and long exposure images for 1900V and pressures (b) 1000 mbar, (b) 500 mbar and (c) 200 mbar.

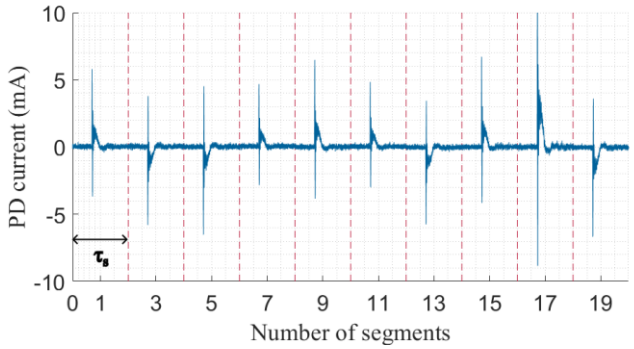

Fig. 12. Plot for cable E-AWG22, position A, 1900 V, and 1000 mbar showing the first 10 acquired segments containing the PD pulses with τ_s = 2 µs time window.

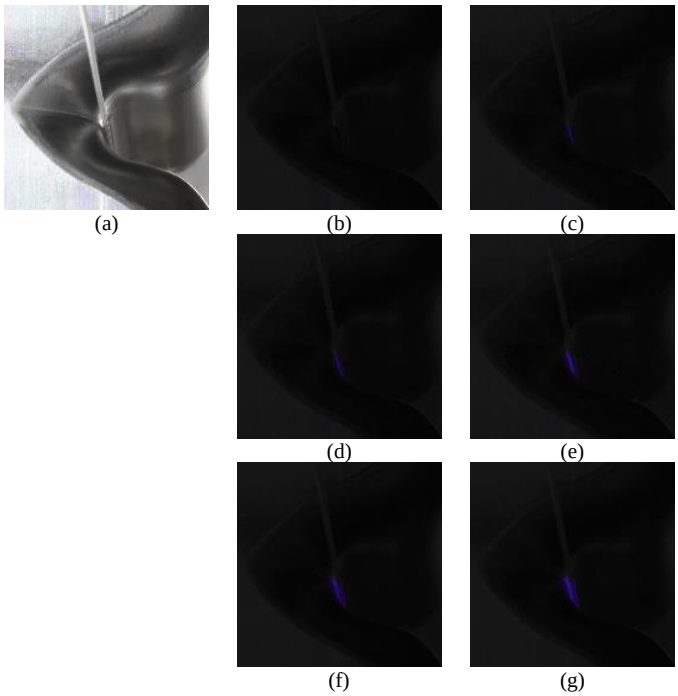

(a) (b) (c) (d) (e) (f) (g)

Fig. 13. Position A - brightfield (a) and long exposure images:
1000 mbar at (b) PDIV, (c) PDIV+20%,
500 mbar at (d) PDIV, (e) PDIV+20%,
200 mbar at (f) PDIV, (g) PDIV+20%.

possibly accurately detect such pulses but in this case the DSLR camera was used to pinpoint the location of the discharges and their spatial distribution rather than their occurrence.

Fig. 13 – Fig. 15 present the images captured at PDIV and PDIV +20%, across varying pressures and positions. The

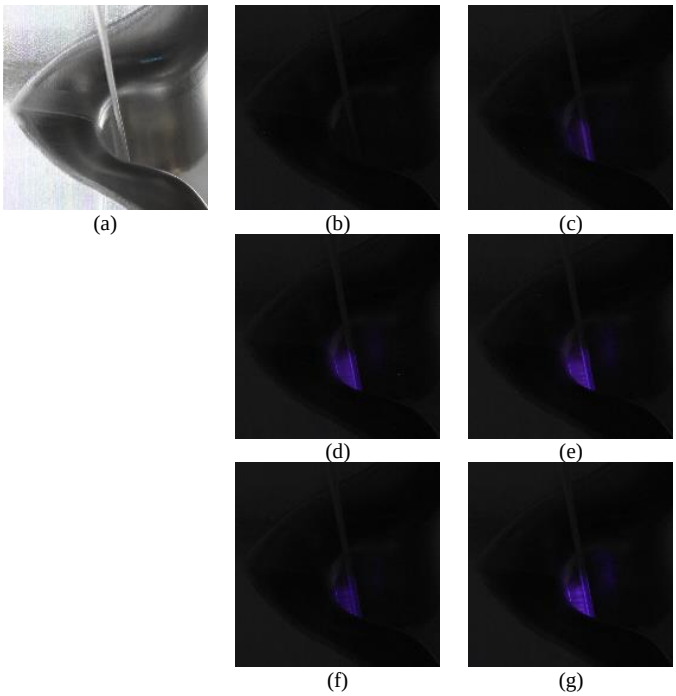

(a) (b) (c) (d) (e) (f) (g)

Fig. 14. Position B - brightfield (a) and long exposure images:
1000 mbar at (b) PDIV, (c) PDIV+20%,
500 mbar at (d) PDIV, (e) PDIV+20%,
200 mbar at (f) PDIV, (g) PDIV+20%.

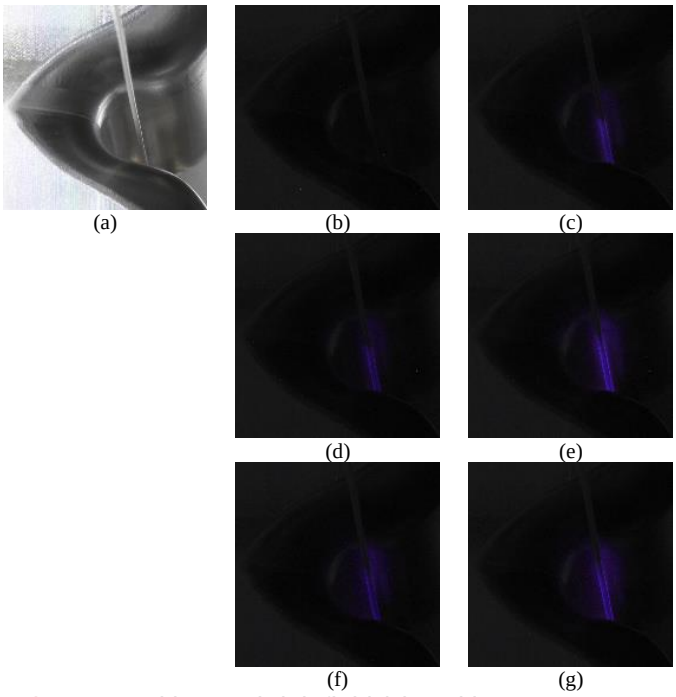

(a) (b) (c) (d) (e) (f) (g)

Fig. 15. Position E - brightfield (a) and long exposure images:
1000 mbar at (b) PDIV, (c) PDIV+20%,
500 mbar at (d) PDIV, (e) PDIV+20%,
200 mbar at (f) PDIV, (g) PDIV+20%.

observations indicate an intriguing relationship: even though the value of PDIV at lower pressures is lower than that at higher pressures, the captured light intensity is greater. This higher

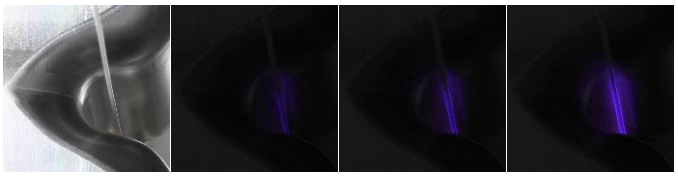

(a) (b) (c) (d)

Fig. 16. Position E (a) bright field image and long exposure images for 200 mbar and (b) PDIV, (c) PDIV + 25% and (c) PDIV + 60%.

intensity suggests more energetic discharges or higher repetition rate, pointing to a potentially more harmful effect on the system. The analysis of this study indicates that PD pulses captured at lower pressures exhibit longer durations, and higher mean PD current suggesting increased energy levels. The pulse repetition rate was slightly increased with decreasing pressure. This can be attributed to the extension of the mean free path of electrons in low-pressure environments, which leads to a reduced frequency of collisions between electrons and gas molecules. Consequently, this decrease in collisional interactions enables an increase in the kinetic energy of electrons. It should be noted that a more pronounced difference in repetition rate might emerge if voltages of higher frequencies were applied, as seen in [15]. From the figures, it is also observed that a 20% increase in voltage further intensifies the activity, a result that aligns with expectations. These findings agree with the work in [16] and contribute to a nuanced understanding of how pressure and voltage levels interact with partial discharge behaviour, with important implications for system safety and reliability.

Adjusting the cable offset from the ground electrode leads to evident differences in behaviour, as demonstrated when moving from position B to the coaxial position E for identical pressure levels. In Fig. 14 (g), the activity between the cable and the electrode appears to almost bridge the air gap, a phenomenon not observed in Fig. 15 (g). This observation is highly significant, as it highlights the potential impact that different positions of a cable within a channel might have on partial discharges. Understanding this effect is critical, especially in the context of complex configurations like cable bundles, where interactions may be more multifaceted. Therefore, replicating these tests with a bundle would be an important next step in exploring these interactions more thoroughly.

Upon subjecting the cable to higher voltages, a significant amount of light emitted from partial discharges was captured by the camera, as illustrated in Fig. 16. The PD activity at PDIV level, as well as at PDIV + 25% and PDIV + 60%, can be observed. Further analysis of the images shown in Fig. 11 and Fig. 16 reveals how the pixel intensity escalates with a decrease in pressure (Fig. 17) or an increase in voltage (Fig. 18). The values are normalized based on the maximum value observed across the three cases examined.

C. Comparison with Established Equations

The Paschen curve, as depicted in Fig. 19 and given by (2) [17], serves as a crucial criterion for determining cable

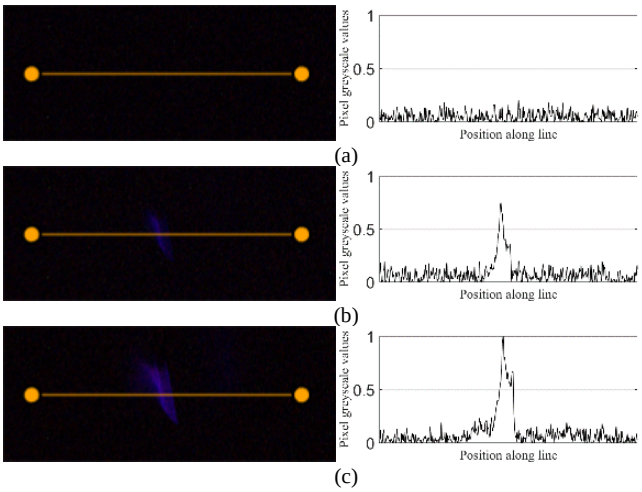

Fig. 17. Pixel intensity plots for position A, 1900 V and pressures: (a) 1000 mbar, (b) 500 mbar and (c) 200mbar.

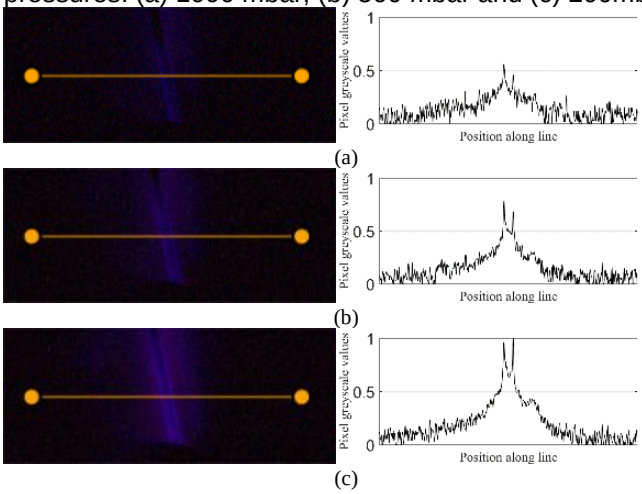

Fig. 18. Pixel intensity plots for position E, 200 mbar and (a) PDIV, (b) PDIV + 25% and (c) PDIV + 60%.

clearances [18] within the aircraft power system, particularly for uniform electric field distributions. This concept, grounded in the Paschen law, illustrates the relationship between the electric breakdown voltage and pressure-distance product in a gas, and has profound implications for insulation design in high-voltage systems.

$$V_b = \frac{B * p * d}{\ln \frac{A * p * d}{\ln(1 + {}^{1}/_{\gamma})}} \qquad (2)$$

Where p represents the pressure of the gas, d signifies the distance between the energized and the grounded electrode and coefficients A and B are experimentally obtained and vary for different gases. In air, the commonly accepted values found in literature are A=12 Torr-1cm-1 and B=365 Vcm-1. The factor γ depends on the electrode material and its value is also calculated experimentally. In literature, it is often taken as $\gamma=10^{-2}$ for aluminium [19].

Fig. 20 presents curves derived from Halleck's proposed formula given by (3) [20] to predict PDIV, a method that has been widely utilized in various works [20] - [24] for cable performance assessment and insulation systems in general.

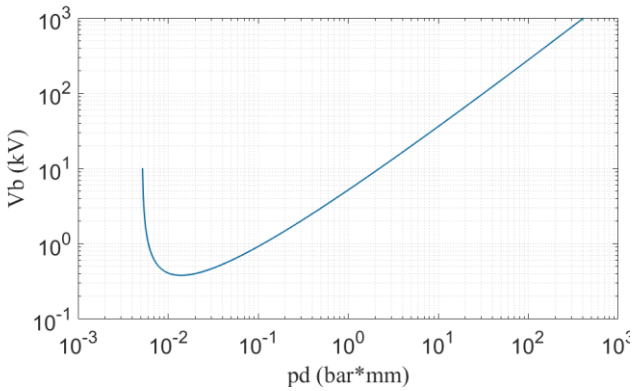

Fig. 19. Paschen curve for air at variable pressure and distance.

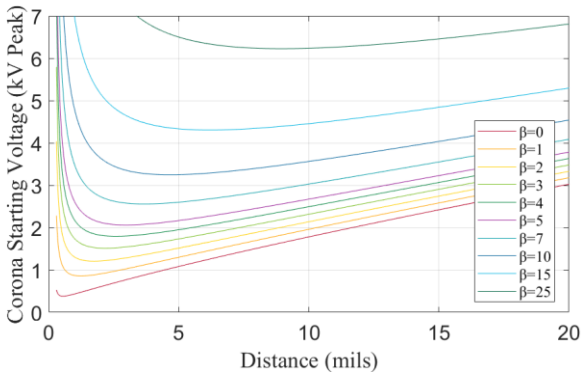

Fig. 20. Halleck curves for variable β and distance.

$$V = V_s * \left(1 + {}^{\beta}/_{d}\right) \quad (3)$$

Where V is the corona-starting voltage, Vs is the spark breakdown voltage for the air gap d and β represents the ratio d/ε_d, where ε_d is the dielectric constant of the material under test. Indeed, a comparable methodology is employed in Aerospace Standard [26] for determining the appropriate insulation thickness of aircraft wiring.

In this section, the applicability of these equations for predicting PDIV will be thoroughly explored for the specific cables tested in this work, particularly focusing on coaxial geometries. The aim is to ascertain whether these generalized models can accurately represent the complex interplay of factors affecting PDIV in the coaxial geometry and conditions of the studied cables.

It was shown in section III-A that the cables exhibit different values in each case, reflecting distinct performance characteristics. However, they all follow the same trend, whether by varying only the pressure while keeping the offset from the electrode constant, or by maintaining constant pressure while altering the position.

Fig. 21 illustrates the average values with their corresponding standard deviations and the fitted curve derived from the minimum values obtained for Position B while varying the pressure. In the same plot, the Paschen curve is drawn for a fixed distance that corresponds to the same air gap created by Position B (3 mm). The Halleck curve is also plotted, taking into consideration the same variables, as well as factoring in a

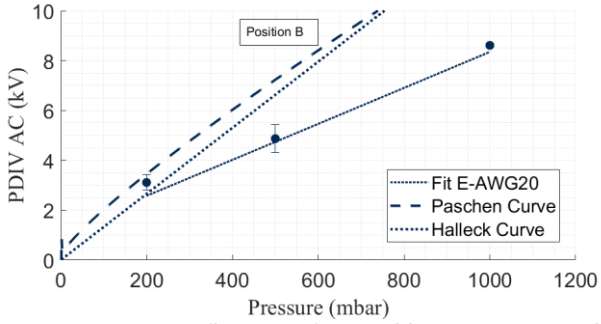

Fig. 21. E-AWG20 fit curve for position B - Comparison with Paschen and Halleck curves for dielectric constant 2.1 and thickness=0.18mm.

dielectric constant of 2.1 and an insulation thickness of 0.18 mm. These parameters correspond to the actual values for the E-AWG20 cable, making the comparison more precise and contextually relevant. This comparison supports a deeper understanding of the cable's behaviour in relation to established models, providing insights that may guide further research and practical applications.

This offers a clear illustration of how the actual PDIV values, the Paschen curve and the Halleck curve interact at different pressure levels. Specifically, at lower pressures such as 200 mbar, the curves almost coincide. However, as the pressure increases, a noticeable offset between the curves appears, with the actual PDIV values falling significantly below those predicted by the Paschen and Halleck formulae. This divergence suggests that the traditional Paschen and Halleck equations do not fully capture the complex behaviours exhibited by the cables at higher pressure levels in coaxial geometries.

D. Derivation of Empirical Formula for Critical Voltage

Working from the reference Fig. 22 (a), for a dielectric thickness of 0mm (bare wire) the electric potential is given at all points in the space by:

$$\phi(r) = -E(r) r\, ln(r) + \phi_0 \quad (4)$$

Integrating (4) between the limits (b and α), at the critical electric field in air E_{cr} the critical applied voltage is:

$$V_{cr} = E_{cr} a \left[\ln\left(1 + \frac{d}{a}\right)\right] \quad (5)$$

Upon including a dielectric layer as in Fig. 22 (b), the surface potential at the interface between the dielectric and the air is calculated by considering the electric field at the radial distance $r=\alpha+t_d$, where t_d is the dielectric thickness. The surface potential $\phi_{\alpha+td}$ is then derived as:

$$\phi(a + t_d) = -E_{(a+t_d)}(a + t_d)\, ln(a + t_d) + \phi_0 \quad (6)$$

This potential, denoted as V_{surf} when evaluated at $r=\alpha+t_d$, gives the critical surface voltage $V_{surf\_cr.}$

$$V_{surf\_cr} = E_{cr}(t_d + a) \ln\left(1 + \frac{d}{t_d + a}\right) \quad (7)$$

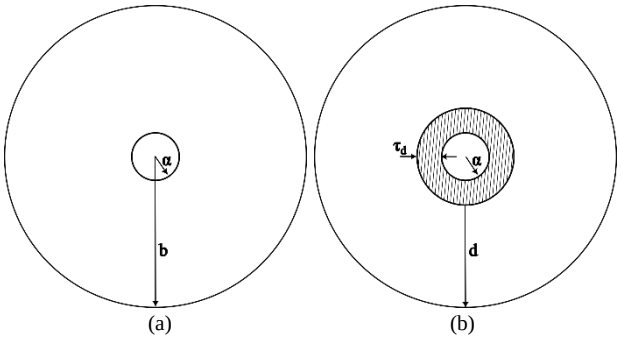

Fig. 22. Reference coaxial geometry with (a) inner conductor radius α, outer condor radius b and (b), conductor radius α insulation thickness t_d, and offset from electrode surface d.

The surface potential is related to the conductor voltage by integrating the electric field from the outer conductor toward the centre. The ratio of the conductor voltage to the surface potential is given by k, which is a dimensionless factor accounting for the logarithmic potential distribution across the dielectric layer and the air gap:

$$\frac{V}{V_{surf}} = 1 + \frac{1}{\varepsilon_r} \cdot \frac{\ln\left(1 + \frac{t_d}{a}\right)}{\ln\left(1 + \frac{d}{a + t_d}\right)} = k \tag{8}$$

Where ε_r is the dielectric constant.

Finally, the critical applied voltage is determined by multiplying the critical surface voltage by the correction factor k:

$$V_{cr} = k \cdot V_{surf\_cr} \tag{9}$$

The critical field E_{cr1} is obtained using Peek's formula [27]

$$E_{cr1} = 30 \cdot \delta \cdot \left[1 + \frac{0.3}{(\delta \cdot \alpha)^{1/2}}\right] \tag{10}$$

If an equivalent radius of $\alpha+t_d$ is assumed, E_{cr2} is obtained. This adjustment assumes that corona discharge will initiate in the air, so the effective radius of the conductor is increased by the presence of the insulation. Hence the formula becomes:

$$E_{cr2} = 30 \cdot \delta \cdot \left[1 + \frac{0.3}{(\delta \cdot (\alpha + t_d))^{1/2}}\right] \tag{11}$$

Where δ is the relative air density and given by:

$$\delta = \frac{P}{P_0} \cdot \frac{273 + T_0}{273 + T} \tag{12}$$

With P_0 typically being 1013 mbar and T_0 the standard temperature of 20°C.

Using this empirical approach, the values of the critical applied voltages V_{cr1} and V_{cr2} at different pressures, specifically at 1000, 500, and 200 mbar, are compared with the established Paschen and Halleck curves, as well as with experimental data in Fig. 23.

It is noteworthy to mention that alongside the empirical method, an attempt was made to utilize a first-principles approach to compute the field enhancement factor, which would then be applied in conjunction with the Paschen law to estimate the critical voltage. However, the results obtained from the first-principles method did not yield a satisfactory correlation with the empirical findings, indicating that the formula provided by Peek remains a more reliable predictor in this context.

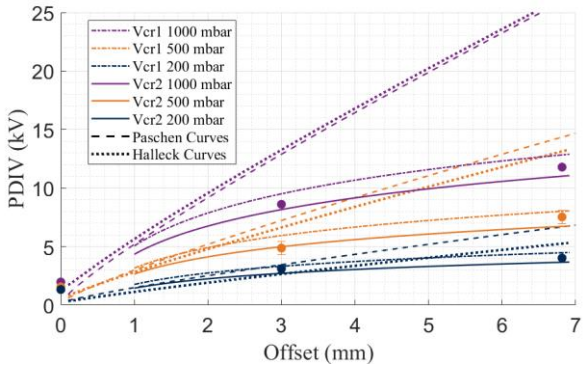

Fig. 23. Comparison of proposed models for different pressures with experimental data of E-AWG20 cable and Paschen and Halleck curves for offset being the air gap, dielectric constant 2.1 and thickness=0.18mm.

The deviation between the fitted curves and the formulae provided by Paschen and Halleck is apparent. The divergence between the curves becomes more pronounced as the pressure increases. The proposed models demonstrate a significantly closer correlation to the experimental data. Future research could focus on conducting a sensitivity analysis of the models to explore its performance across varying material properties and thicknesses. This would not only broaden the understanding of the model's applicability but also contribute to refining its accuracy through the aggregation of additional data.

IV. Conclusion

This study has investigated and clarified the complexities of aeronautical cable performance in coaxial geometries under various pressure and positional conditions. Findings have highlighted significant deviations from traditional predictive models such as Paschen's curve and Halleck's method, prompting the proposal of a new model. The investigation revealed that both increased pressure and offset lead to a rise in PDIV, with distinct linear and logarithmic trends observed for each factor. Furthermore, the use of long-exposure imaging has unveiled the potential effects of cable positioning within a channel on partial discharge phenomena. These insights necessitate a nuanced examination of each variable's impact within this specialized geometry, paving the way for future research to enhance the predictive accuracy and reliability of aeronautical cable systems.

References

[1] M. Lizcano, T. S. Williams, E.-S. E. Shin, D. Santiago, and B. Nguyen, 'Aerospace Environmental Challenges for Electrical Insulation and Recent Developments for Electrified Aircraft', *Materials*, vol. 15, no. 22, p. 8121, Nov. 2022, doi: 10.3390/ma15228121.

[2] L. Lusuardi, A. Rumi, G. Neretti, P. Seri, and A. Cavallini, 'Assessing the severity of partial discharges in aerospace applications', in *2019 IEEE Conference on Electrical Insulation and Dielectric Phenomena (CEIDP)*, IEEE, Oct. 2019, pp. 267–270. doi: 10.1109/CEIDP47102.2019.9009970.

[3] Y. Ji *et al.*, 'Moving Towards Partial Discharge-Free Design of Electrical Machines for More Electric Aircraft Applications', *IEEE Transactions on Transportation Electrification*, pp. 1–1, 2023, doi: 10.1109/TTE.2023.3248154.

[4] Th. Lebey, A. Rumi, and A. Cavallini, 'Challenges for Electrical Insulation Systems in High Voltage Aviation Applications', *IEEE Electrical Insulation Magazine*, vol. 38, no. 6, pp. 5–11, Nov. 2022, doi: 10.1109/MEI.2022.9916178.

[5] J.-R. Riba, Á. Gómez-Pau, and M. Moreno-Eguilaz, 'Insulation Failure Quantification Based on the Energy of Digital Images Using Low-Cost Imaging Sensors', *Sensors*, vol. 20, no. 24, p. 7219, Dec. 2020, doi: 10.3390/s20247219.

[6] W. Khachen, J. Suthar, A. Stokes, R. Dollinger, and W. G. Dunbar, 'Aerospace-specific design guidelines for electrical insulation', *IEEE Transactions on Electrical Insulation*, vol. 28, no. 5, pp. 876–886, 1993, doi: 10.1109/14.237748.

[7] F. W. Peek, *Dielectric Phenomena in HV Engineering*. New York: McGraw-Hill, 1929.

[8] P. N. Mikropoulos and V. N. Zagkanas, 'Modelling of positive corona inception in the coaxial cylindrical electrode arrangement under variable air density', in *17th International Symposium on High Voltage Engineering*, 2011.

[9] G. Hartmann, 'Theoretical Evaluation of Peek's Law', *IEEE Trans Ind Appl*, vol. 20, no. 6, pp. 1647–1651, 1984.

[10] R. T. Waters and W. B. Stark, 'Characteristics of the stabilized glow discharge in air', *J Phys D Appl Phys*, vol. 8, no. 4, pp. 416–426, Mar. 1975, doi: 10.1088/0022-3727/8/4/014.

[11] J. A. Harrison, 'A computer study of uniform-field electrodes', *British Journal of Applied Physics*, vol. 18, no. 11, pp. 1617–1627, Nov. 1967, doi: 10.1088/0508-3443/18/11/316.

[12] BSI, 'BS EN 60270: High-Voltage Test Techniques - Partial Discharge Measurements', 2001.

[13] BSI, 'BS EN 3475: Aerospace series-Cables, electrical, aircraft use-Test methods Part 307: Corona extinction voltage', 2015. doi: https://doi.org/10.3403/30298619U.

[14] G. Lopez, 'High-Performance Polymers for Aeronautic Wires Insulation: Current Uses and Future Prospects', *Recent Prog Mater*, vol. 3, no. 1, Feb. 2021, doi: 10.21926/rpm.2101005.

[15] J. Jiang, B. Zhang, Z. Li, C. Zhang, P. Ranjan, and X. Zhang, 'Partial Discharge Investigation under Low Air Pressure and Variable Frequency for More-electric-aircraft', *IEEE Transactions on Dielectrics and Electrical Insulation*, vol. 28, no. 5, pp. 1793–1801, Oct. 2021, doi: 10.1109/TDEI.2021.009639.

[16] P. Bas-Calopa, J.-R. Riba, and J. A. Ortega, 'Low-Pressure Optical Detection, Location, and Quantification of Electrical Discharges in Aircraft Wiring Systems', *Aerospace*, vol. 10, no. 1, p. 3, Dec. 2022, doi: 10.3390/aerospace10010003.

[17] E. Kuffel, W. S. Zaengl, and J. Kuffel, *High Voltage Engineering Fundamentals*. Elsevier, 2000. doi: 10.1016/B978-0-7506-3634-6.X5000-X.

[18] R. Rui and I. Cotton, 'Impact of low pressure aerospace environment on machine winding insulation', in *2010 IEEE International Symposium on Electrical Insulation*, IEEE, Jun. 2010, pp. 1–5. doi: 10.1109/ELINSL.2010.5549718.

[19] A. J. Nelms, 'ELECTRICAL DISCHARGE IN THE MORE ELECTRIC AIRCRAFT POWER SYSTEM', 2007.

[20] M. C. Halleck, 'Calculation of Corona-Starting Voltage in Air-Solid Dielectric Systems', *Transactions of the American Institute of Electrical Engineers. Part III: Power Apparatus and Systems*, vol. 75, no. 3, Jan. 1956, doi: 10.1109/AIEEPAS.1956.4499294.

[21] I. Cotton, R. Gardner, D. Schweickart, D. Grosean, and C. Severns, 'Design considerations for higher electrical power system voltages in aerospace vehicles', in *2016 IEEE International Power Modulator and High Voltage Conference (IPMHVC)*, IEEE, Jul. 2016, pp. 57–61. doi: 10.1109/IPMHVC.2016.8012771.

[22] P. Narbut, D. Berg, C. N. Works, and T. W. Dakin, 'Factors Controlling Electric Strength of Gaseous Insulation', *Transactions of the American Institute of Electrical Engineers. Part III: Power Apparatus and Systems*, vol. 78, no. 3, pp. 545–550, Apr. 1959, doi: 10.1109/AIEEPAS.1959.4500375.

[23] H. Xu, R. Lowndes, and I. Cotton, 'Power Capacity of High Voltage Cables for Future Electrical Aircraft', in *2021 IEEE Electrical Insulation Conference (EIC)*, IEEE, Jun. 2021, pp. 177–180. doi: 10.1109/EIC49891.2021.9612313.

[24] R. Acheen, T. Lebey, G. Belijar, Y. Pelletier, O. Petit, and D. Berthier, 'Risk Assessment of PD Inception in Aeronautic Cables & Connectors in View of the Voltage Increase in Aviation Applications', in *2023 INSUCON - 14th International Electrical Insulation Conference (INSUCON), Birmingham, United Kingdom*, 2023, pp. 33–38.

[25] E. Husain and R. S. Nema, 'Surface Discharge Studies with Uniform Field Electrodes at Low Pressures', *IEEE Transactions on Electrical Insulation*, vol. EI-16, no. 2, pp. 128–133, Apr. 1981, doi: 10.1109/TEI.1981.298352.

[26] AS50881 SAE International Technical Standards and Aerospace Group, 'Wiring Aerospace Vehicle', 2023.

[27] J. J. Lowke and F. D'Alessandro, 'Onset corona fields and electrical breakdown criteria', *J Phys D Appl Phys*, vol. 36, no. 21, pp. 2673–2682, Nov. 2003, doi: 10.1088/0022-3727/36/21/013.